Acta Materialia 297 (2025) 121321

Contents lists available at ScienceDirect

Acta Materialia

journal homepage: www.elsevier.com/locate/actamat

Crystal plasticity parameter identification via statistical relevant micropillar compression

Niklas C. Fehlemann [a,*], Angelica Medina [b], Subin Lee [b], Christoph Kirchlechner [b], Sebastian Münstermann [a]

[a] Institute of Metal Forming, RWTH Aachen University, Intzestrasse 10, Aachen, 52074, Germany
[b] Institute for Applied Materials, Karlsruhe Institute of Technology, Kaiserstraße 12, Karlsruhe, 76131, Germany

ARTICLE INFO

Dataset link: https://github.com/ibf-RWTH

Keywords:
crystal plasticity
representative volume elemen
micropillar compression
dual phase steel

ABSTRACT

In order to predict ductile damage initiation at the microstructure level, especially for multi-phase materials, it is essential to have high-fidelity crystal plasticity parameters. They need to accurately represent the evolving phase contrast, which implies that the initial phase contrast and the individual strain hardening of the phases has to be mapped precisely. This paper presents a methodology for calibrating the parameters of a phenomenological crystal plasticity model for a DP800 steel based on the critical resolved shear stress from *in situ* micropillar compression tests taken out of macroscopic tensile tests at various prestrain levels. Furthermore, the influence of mechanical size effects was incorporated through the inclusion of statistical relevant micropillar compression tests of varying prestrains and dimensions. The data were used to calibrate a model, which successfully predicted the homogenized macroscopic stress–strain curve from uniaxial tensile tests with a mean absolute error of only 20.7 ± 7.7 MPa and a mean absolute percentage error of 3.3%. Furthermore, it was shown that the influence of the strain hardening of the martensite can be neglected under certain conditions, especially when predicting the homogenized stress response for low strains. This result demonstrates the importance of high-fidelity parameter calibration for damage prediction, when compared to a synthetic parameter set, which leads to a different stress and strain partitioning for the same homogenized stress–strain curve.

1. Introduction

The availability of high-fidelity material models is of particular importance for the accurate numerical prediction of material behavior at different scales. This calls for not only the numerical models themselves, but also for validated parameter sets and identification strategies. In the case of material models that represent the homogenized mechanical behavior of a single phase polycrystalline bulk material, simple macroscopic tests, such as tension, compression, or similar can be employed, which are comparably easy to conduct and to be integrated in automated calibration schemes [1–3].

In the case of material models at the microstructural length scale, such as constitutive crystal plasticity (CP) models [4,5], it is necessary to map the mechanical properties of individual phases. This presents a unique challenge, as the mechanisms of plasticity at the microstructural length scale are intricate and the extraction of crucial properties such as yield stress or strain hardening behavior is often not feasible without interference [6,7]. In particular, when assessing the micromechanical sources of damage, high-fidelity parameters are needed, as the local phenomena of damage initiation and evolution are linked upon a variety of influencing variables. These include phase contrast, microstructure morphology and the strain hardening of individual phases [8–11]. Tian et al. [12] demonstrated that the discrepancy in damage behavior between two macroscopically equivalent dual-phase steels can be attributed to mechanical heterogeneity, which is primarily influenced by the *hardening of ferrite* and the initial *phase contrast* between ferrite and martensite. Furthermore, de Geus et al. [13] observed that the mechanical response of a material is predominantly governed by the phase contrast, especially if the phase contrast is comparably low. This underscores the call for high-fidelity material parameters to accurately quantify these effects.

There are multiple approaches for the calibration of CP models: For the majority of the approaches, representative volume elements (RVE) are typically employed to represent the polycrystalline material. An RVE is defined as a mapping of relevant microstructural features for which the following condition holds: $L_{micro} \ll L_{RVE} \ll L_{macro}$ [14], where L_x denotes the respective length scale. The data basis of these models is comprised of two- and three-dimensional microstructure images obtained through electron backscatter diffraction (EBSD) or

* Corresponding author.
E-mail address: niklas.fehlemann@ibf.rwth-aachen.de (N.C. Fehlemann).

https://doi.org/10.1016/j.actamat.2025.121321
Received 6 April 2025; Received in revised form 4 July 2025; Accepted 9 July 2025
Available online 22 July 2025

scanning electron microscopy (SEM) images of sufficient size [15]. A straightforward method for the subsequent calibration is the utilization of uniaxial, macroscopic tensile or compression tests in conjunction with RVE, accompanied by an iterative adjustment of the crystal plasticity parameters to fit the global stress–strain curve [16–20]. A typical problem here is the non-uniqueness of the identified parameter sets. Sedighiani et al. [16] used genetic algorithms for the calibration of a phenomenological and a physics-guided dislocation density crystal plasticity model. The results demonstrated that the majority of model parameters exerts no unique impact, indicating that the effect of a particular parameter can be compensated for by the suitable selection of other parameters. This problem is further multiplied when a multi-phase material is examined. Here, the parameter selection also influences the local heterogeneity of the different phases.

A micromechanical testing method suitable for the calibration of crystal plasticity models is an instrumented nanoindenter. This method permits the examination of individual grains within a bulk sample. Generally, it is feasible to derive single-phase flow curves directly from nanoindentations conducted with a spherical indenter, as shown be Leitner et al. [21]. An alternative approach is to inversely calibrate the constitutive model parameters based on a Finite-Element (FE) model of the nanoindentation experiment. Zambaldi et al. and Tasan et al. employed a combination of nanoindentations, EBSD measurements, and atomic force measurements to identify the constitutive parameters of both hexagonal titanium [22] and the ferrite phase of a commercial dual-phase steel DP800 [23]. In the second case, the constitutive parameters of the martensite were determined by a subsequent inverse fit to the macroscopic stress–strain curve. In both cases, as well as in Chakraborty and Eisenlohr [24], the parameter sets were not validated with macroscopic tests. Thus, the transferability to RVE simulations is not fully proven. When calibrating multi-phase materials with the aid of the macroscopic stress–strain curves there is also no validation test available. An additional approach using nanoindentation was proposed by Gallardo-Basile et al. [25]. They utilized the discrepancy between the experimental and simulative post-mortem imprint of the nanoindent as the target value for the parameter identification. The critical resolved shear stress (CRSS) measured by *in situ* micropillar compression was employed as the upper bound for the corresponding material parameter, thereby stabilizing the parameter calibration. It was demonstrated that it is feasible to predict the macroscopic stress–strain curve for a single-phase ferritic material. However, it was shown that in the absence of constraints on the CRSS from the micropillar, a considerable overestimation of the macroscopic flow curve occurs.

An additional approach for estimating the flow and hardening behavior is based on the local chemical composition [26,27]. This model is mostly empirical, although aspects of dislocation theories are included. Vajraguta et al. [28] employed this methodology to model the individual flow curves of ferrite and martensite in a DP600 steel, resulting in a compelling approximation of the flow curve of the bulk material. However, a limitation of this approach is the larger number of parameters, necessitating careful selection, as well as the limited accuracy while solely relying on the chemical composition and not other factors like e.g. thermomechanical treatments.

Lastly, micropillar compression experiments can be employed. Ghassemi-Armaki et al. [29] conducted a parameter identification for a dislocation-based CP model for a fully martensitic steel. They observed that the yield stress of the material was not affected by the size of the micropillar, which they attributed to the presence of multiple martensite blocks inside the individual pillars. In contrast to this finding, significant size effects are frequently observed in micropillar tests on single-crystals based on experiments and molecular dynamics [30,31] or discrete dislocation dynamics simulations [32,33]. These size effects and the fact that the stress–strain curve is influenced by free surfaces, especially in single-phase micropillar tests, make it almost impossible to calibrate classical CP models on these tests.

In general, the majority of calibration approaches do not consider the impact of size effects, which have been empirically validated for polycrystalline steels through the well-known Hall–Petch relationship [34,35]. To model these size effects in micropillar or polycrystalline simulations as well, mechanism-based, gradient-extended CP models can be employed [36–39]. However, due to the high computation times of these models, Wu et al. [40] utilized an approach based on the Hall–Petch relationship to scale the critical resolved shear stress parameter τ_0 using the corresponding grain diameter in the RVE. The parameters of the Hall–Petch equation were determined through the use of nanoindentations on grains of varying sizes.

All presented approaches have different disadvantages in the calibration of parameters, which are necessary for the accurate modeling of local mechanical heterogeneity of multi-phase materials. Therefore, this paper presents a novel methodology for parameter identification that can be applied to a multi-phase material without data from the macroscale, which is then used for the validation of the calibrated parameters. The chosen use case is to calibrate model parameters of a phenomenological CP model for a dual-phase steel DP800. The methodology is capable of accurately mapping the phase contrast and the hardening of the ferrite, two variables that are of significant importance for the damage tolerance of the material. The data used in this study is based on *in situ* micropillar compression tests on prestrained tensile specimens conducted by Tian et al. [12]. Section 2.1 presents the experimental data basis, followed by the utilized CP model in Section 2.2 and the presentation of the RVE 2.3 and the calibration strategy 2.4. Section 3 shows the results, while Section 4 discusses the most important findings. Finally, an outlook and summary are given.

2. Experimental and numerical methodology

2.1. Material properties

The material used in this study is a standard commercially available DP800 dual-phase steel. Further details on the material can be found for example in Wollenweber et al. [41],Kusche et al. [42]. The microstructure consists of ferrite and martensite, with average grain sizes of approximately 6.5 ± 0.1 µm and 1.0 ± 0.1 µm, respectively. The macroscopic mechanical properties were determined through quasistatic, uniaxial tensile testing of specimen oriented along the rolling direction (RD). Five specimens were tested, and the strain data was obtained without contact using a video extensometer. The raw data is not shown in this paper, but can be found alongside the other data at: https://github.com/ibf-RWTH.

To measure the CRSS of ferrite and the yield strength of martensite, micropillar compression tests were used (Fig. 1a)). As it is not possible to quantify the strain hardening of ferrite from single-crystal micropillar compression as this is skewed by the free surfaces of the single-phase micropillar [6], it was measured employing *in situ* SEM micropillar compression on several differently prestrained macro samples [12]. Micropillars with diameters ranging from 1–3 µm for ferrite and up to 800 nm for martensite were fabricated using a dual-beam focused ion beam (FIB) on an OPS-polished sample surface. They were milled employing a three-step milling process using 30 keV Ga+ ions: rough milling with 16 nA, intermediate milling with 2 nA, and final polishing with 240 pA. The resulting micropillars had an aspect ratio (height/diameter) ranging from 2 to 4. *In situ* compression tests were conducted at a loading rate of 0.001 s^{-1}. The CRSS of ferrite was determined using the measured 0.2% offset yield strength and the Schmid factor of the activated slip system. With a sufficiently large number of these experiments, the empirical cumulative density function (ECDF) of the CRSS for different prestrain levels (see Fig. 1b)), as well as the mean hardening of the ferrite, can be approximated. Due to the limited plasticity of martensite, its yield strength at 0.2% offset was determined instead of CRSS. These investigations build the foundation for the parameter identification strategy in this paper.

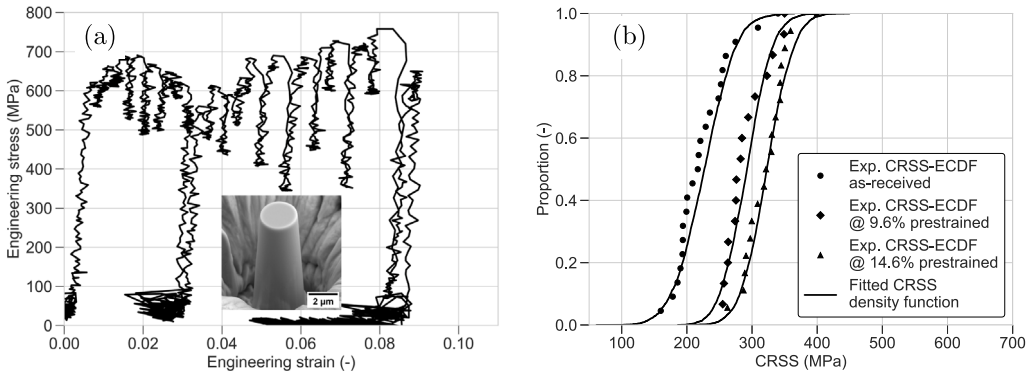

Fig. 1. Micropillar compression experiments for assessing the critical resolved shear stress. (a) Representative stress–strain curve from pillar compression experiment, (b) ECDF of the ferrite CRSS at different prestrain levels.

2.2. Crystal plasticity modeling

To map the experimentally determined hardening to numerical models and predict macroscopic behavior, a crystal plasticity model is needed. In this study, the open-source, multi-physics framework DAMASK [43] is used. DAMASK offers a variety of models for the description of plasticity, damage and thermal effects at the micro level, which are integrated with a diverse palette of numerical solvers. In this study, a phenomenological crystal plasticity model in combination with a Fast Fourier transformation (FFT) backed spectral solver was employed. The original formulation of phenomenological crystal plasticity, which dates back to the 1970s, was developed by Rice, Hutchinson, and Peirce [44–47]. The fundamental principle of the model family is the decomposition of the deformation gradient F into its constituent parts:

$$F = F_e F_p F_i \tag{1}$$

$$\dot{F}_p = L_p F_p \tag{2}$$

Here, F_e is the elastic, F_p the plastic and F_i the inelastic part of the deformation gradient. The inelastic part is mainly caused by effects such as crack opening or thermal expansion [48] and not further considered in this study. The evolution of the plastic deformation (Eq. (2)) is controlled by the plastic velocity gradient L_p, which is calculated as follows:

$$L_p = \sum_{\alpha=1}^{N} \dot{\gamma}^{\alpha}(\vec{m}^{\alpha} \otimes \vec{n}^{\alpha}) \tag{3}$$

N is the number of active slip systems, $\dot{\gamma}^{\alpha}(\xi^{\alpha})$ the shear rate on slip system α. $\vec{m}$ and $\vec{n}$ are the unit vectors for the slip direction and the normal of the slip plane. The shear rate γ^{α} is calculated based on the resolved shear stress ξ^{α} (ξ is the notation in DAMASK, often τ is used instead):

$$\dot{\gamma}^{\alpha} = \dot{\gamma}_0 \left| \frac{\xi^{\alpha}}{\xi_c^{\alpha}} \right|^{n} sign(\xi^{\alpha}) \tag{4}$$

ξ^{α} denotes the slip resistance on a slip system α. The reference shear rate $\dot{\gamma}_0$ and m are material parameters which have to be calibrated. The effect of the hardening in slip system β on the hardening of slip system α can be written as follows:

$$\dot{\xi}_c^{\alpha} = \sum_{\beta=1}^{N} h_{\alpha\beta} \left| \dot{\gamma}^{\beta} \right| \tag{5}$$

$$h_{\alpha\beta} = q_{\alpha\beta} \left[h_0 \left(1 - \frac{\xi_c^{\beta}}{\xi_{\infty}} \right)^{a} \right] \tag{6}$$

Eq. (6) captures the micromechanical interaction in different non-parallel slip systems empirically [5]. h_0, (initial hardening rate) ξ_{∞} (saturation slip resistance) and a (hardening exponent) are material parameters that render the hardening behavior of the single crystal. The matrix $q_{\alpha\beta}$ is a measure for latent hardening with a value of 1 for co-planar slip and 1.4 otherwise. Since the original formulation is only valid for face-centered cubic (fcc) crystals, an extension for body-centered cubic (bcc) crystals is needed, which reads as follows:

$$\xi_{c,bcc}^{\alpha} = \xi_c^{\alpha} + a^{\alpha} \xi_{ng}^{\alpha} \tag{7}$$

where a^{α} is a coefficient to account for the net effect of nonglide (ng) stress on the effective resistance. ξ_{ng}^{α} is the resolved shear stress on the nonglide plane. A comprehensive overview of CP modeling can be accessed in Roters et al. [49]. In addition to the phenomenological models, several models based on dislocation movement are available, which have a larger parameter space but have the advantage that many parameters are known, at least in their order of magnitude. A thorough description of such models can be found in Roters et al. [50] and Ma et al. [51].

In order to model the mechanical behavior of martensite, an isotropic plasticity model was utilized, which is also available in DAMASK [43]. This model is analogous to the phenomenological CP model with regard to its parameters and state variable kinetics. It differs in that it does not consider orientations or slip systems, rendering the model direction-independent. Rendering martensite as a purely elastic phase is not sufficient, as significant plasticity in martensite has been observed in micropillar compression [52]. Since the substructures of martensite are not spatially resolved in the sRVE used (at this resolution, several hundred RVEs would be necessary), the homogenized structures of martensite can be assumed to be isotropic. The isotropic behavior of the martensite is also in line with the experimental data [52].

It should be noted that in order to avoid ambiguity, the experimental and corresponding simulative values are designated by specified nomenclature. In accordance with the conventions established by DAMASK, the notation employed for simulative values is as follows: The material parameter ξ_0 represents the critical resolved shear stress within the model, whereas ξ denotes the evolving shear stress. The Hall–Petch equation for grain size scaling is expressed in the form $\xi_{start} + \frac{k}{d^m}$, whereas m is a size scaling exponent.

2.3. Creation of statistically representative volume elements

To map the microstructure morphology, *statistically* representative volume elements (sRVE) are employed. These sRVE are generated with the self-developed RVE generator DRAGen [53]. DRAGen is capable of mapping intricate microstructural characteristics, including grain shapes and sizes, banded structures, and martensitic or bainitic substructures [53,54]. The specifications of the sRVEs utilized in this study are largely consistent with those described by Pütz et al. [55], and thus, a detailed re-examination of the generation process is not

provided. The phase fraction of the martensite was determined to around 0.3–0.32 based on analysis of SEM images which were imaged using both secondary and backscattered electrons. The images were binarized using the open-source software ImageJ [56], enabling the calculation of the martensite content. Other phases, such as retained austenite or bainite do not exist in this material [57]. EBSD images were taken from all three faces of the sheet material, namely RDxTD, RDxND and TDxND. (ND = normal direction, TD = transverse direction). Using the Matlab toolbox MTEX [58], the morphological grain parameters were calculated by assuming all orientation differences greater than 10° as grain boundaries [58] and then fitting ellipses to the grains. Such an ellipse can be fully described by the area, the aspect ratio and the tilt with respect to the x-axis resp. the rolling direction [54]. This data is used as input for DRAGen. In a two-step process, the grains are first shrinked to 0.4 of their original size and placed randomly in the empty volume. Then, the grains are allowed to grow to their original volume until the sRVE is completely filled. With this, complex microstructural morphology can be reproduced accurately [53]. In addition to the morphological properties of the grains, the crystallographic orientation of the grains is also correctly reproduced in DRAGen. However, the DP800 does not exhibit a strongly pronounced rolling texture due to the intercritical annealing following cold rolling. It should also be noted that grain boundaries are not explicitly present in the approach used. Grain boundaries are only modeled in the form of the orientation differences.

An edge length of 32 µm was selected for the sRVE, which was then discretized into 64 grid points on each edge, resulting in an sRVE with 64^3 points. The size results from the fact that the spectral solver in use is particularly suitable at handling grids of size 2^n, which allows for faster calculations. In accordance with the results outlined by Tian et al. [52], all 48 slip systems were considered active within the simulation framework, but no distinct input distributions of the CRSS were postulated for the various slip systems. To ensure accurate reproduction of the measured statistics, 10 sRVE (comprising 2,953 grains in total, of which 1,000 are ferrite) were generated. Each sRVE is simulated three times with different sets of ξ_0, that were drawn from the distribution already presented in Fig. 1b), resulting in a total of 30 simulations. All sRVE simulations were performed under quasistatic, uniaxial conditions with a strain rate of 0.001 s^{-1}. Unless otherwise specified, the mean and standard deviation of all simulation results are provided in the sections below.

The material parameters of the martensite were also estimated using micropillar tests from [52]. From these experiments, a yield stress of around 3000 MPa was chosen for martensite and reproduced using the aforementioned isotropic plasticity model. A comprehensive calibration of the hardening was not conducted. It is hypothesized that, due to the enormous phase contrast between ferrite and martensite, the effect of the strain hardening of the martensite with respect to the global stress–strain curve is negligible, as the plastic deformation is almost exclusively localized in the ferrite.

2.4. Calibration approach

A two-stage algorithm was employed for the calibration of the CP-model parameters. As the experimentally measured data cannot be transferred directly to the model due to the absence of interface effects, the calibration approach is also an inverse approach. No automatic optimization algorithm is employed; instead, parameter identification is conducted ‘‘by hand’’ using a trial-and-error approach.

Initially, the parameters for the hardening of the ferrite were calibrated: ξ_0-values, which were drawn from the experimentally determined CRSS distribution were assigned to the individual ferrite grains in the sRVE (see Fig. 2a, left part), rendering the model parameter ξ_0 is distinct for each grain. Fig. 2b illustrates this concept by presenting a cross-sectional view of an sRVE. The martensite is represented by a gray color, while the different colors indicate the various ξ_0-values assigned to the ferrite grains. Subsequently, the sRVE were strained up to 0.15 strain, and the values for ξ (the resolved shear stress) were averaged over the individual grains at a strain level of 0.096 and 0.146, yielding a SCDF of ξ for each prestrain-level. These can be compared to the experimentally determined data from the micropillar at the respective prestrain levels of 0.096 and 0.146 (see Fig. 2a, right part). By means of an iterative adjustment of the model parameters a (hardening exponent), h_0 (initial hardening) and ξ_∞ (saturation slip resistance, as a multiple of ξ_0), the hardening in the sRVE was adjusted in such a way that both the mean ξ value (homogenized over the sRVE) and the ξ distributions at both 0.096 and 0.146 are mapped with high accuracy.

Algorithm 1 Algorithm employed for the grain size scaling of ξ_0

Require: Mean CRSS at 1, 2 and 3 μm ξ_1, ξ_2, ξ_3, Mean and Standard deviation of CRSS-Distribution $\mathcal{N}(\mu, \sigma^2)$, List of grain diameters in sRVE M, CRSS at 2 μm $\xi_{2\mu m}$

Calculate Hall–Petch Parameters ξ_{start}, k using least squares regression
$N \leftarrow length(M)$
for $k \leftarrow 1$ to N **do**
  Get grain diameter $d \leftarrow M[k]$
  Calculate x-value $x \leftarrow \frac{1}{\sqrt{d}}$
  Sample $\xi \sim \mathcal{N}(\mu, \sigma^2)$
  Shift y-intercept $\xi_{start} \leftarrow \xi_{start} + (\xi - \xi_{2\mu m})$
  Calculate new $\xi \leftarrow \xi_{start} + kx$
  Assign to grain in sRVE
end for

In order to predict the macroscopic stress–strain curve from the uniaxial tensile test, it is necessary to take into account the effects of grain size on the CRSS and thus the parameter ξ_0 in the model. To this end, an algorithm was formulated that considers both the effects of grain size, employing a Hall–Petch-type scaling approach, and the statistical nature of the CRSS. The methodology is illustrated in Algorithm 1 and Fig. 3. Since Tian et al. [52] have not quantified an individual size scaling law for this steel, the Hall–Petch assumption was used. The question of the transferability of these size-scaling effects is addressed in Section 4. The estimation of these effects was based on the analysis of CRSS-data from micropillar experiments with diameters of 1, 2 and 3 µm. Testing micropillars significantly smaller than the grain size were not part of the previous work, instead, to gain more statistics, a higher number of 3 µm sized pillars was tested. A Hall–Petch regression was then calculated based on the mean CRSS values using least squares regression. To construct the sRVE material input, the previously drawn ξ_0-values assigned to the grains in the sRVE are used to shift the Hall–Petch regression line. This means that for each grain, at first the ξ_0-parameter was taken from the experimentally-determined distribution function, before at second the correction was made to consider the grain size effects according to the Hall–Petch relationship. Fig. 3a shows five different Hall–Petch regression lines as examples, and Fig. 3b illustrates the procedure for a single grain. It should be noted that in this approach, the slope of the individual Hall–Petch regression lines remain constant. The calibration process, which comprises three steps – namely, "Calibration of the strain hardening behavior", "Accounting for grain size effects", and "Validation based on macroscopic data" – is illustrated in a schematic overview in Fig. 4.

Two further parameter studies are conducted using the calibrated model, with a focus on the size scaling exponent m and the hardening of the martensite. The objective of this is to examine the impact of these quantities on the global stress–strain curve and strain localization and partitioning. To this end, sets of sRVE with scaling exponents $m = 0.3$ and $m = 0.7$ were generated and calculated by modifying the grain size scaling approach. The aforementioned investigations allow for the

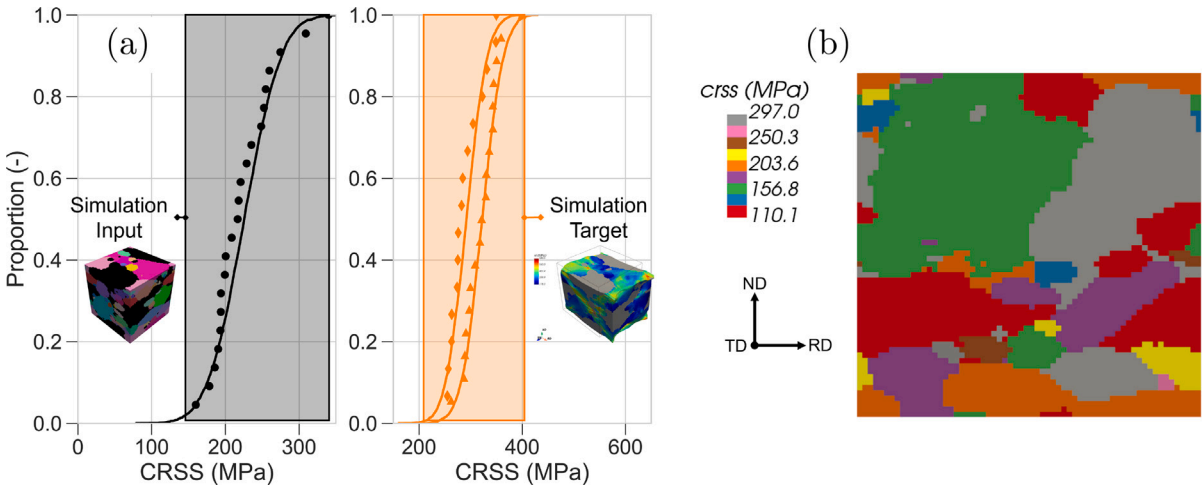

Fig. 2. Approach to map the experimental CRSS-distribution onto the sRVE-model. (a) Experimentally measured CRSS for the "as received" state as input for the sRVE-model (left). CRSS-distributions at the different prestrain levels (right), (b) Slice through an exemplary sRVE. The martensite is shown in gray, while the ferrite grains are shown in different colors due to the different initial ξ_0 value. (For interpretation of the references to color in this figure legend, the reader is referred to the web version of this article.)

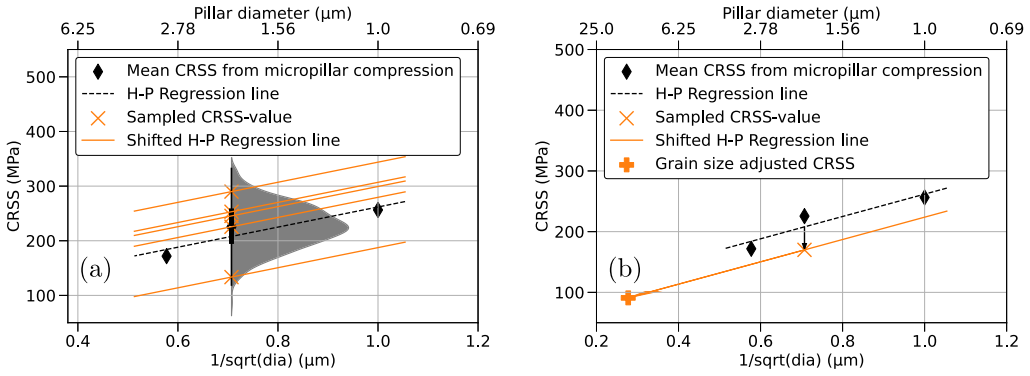

Fig. 3. Graphic description of the grain size scaling algorithm based on the Hall–Petch-relation. (a) Schematic depiction of the shifting of the Hall–Petch regression lines based on the 2 µm pillar CRSS-distribution, (b) Schematic depiction of the calculation of the grain size adjusted ξ_0 material parameter (cf. alg. 1).

Table 1
Calibrated CP-Parameter for ferrite and model parameters for martensite. (* - Fitting parameter for both phases, ** - fitting parameter only for martensite).

	$N(-)$	$n(-)$	$a^*(-)$	h_0^* (MPa)	ξ_0^{**} (MPa)	ξ_∞^* (MPa)
Ferrite	48	20	2.0	230	Sampled	$5 \times \xi_0$
Martensite	–	20	3.25	5000	1000	2000

substantiation of the assumption of $m = 0.5$, which is typically made in the context of the Hall–Petch relation $\xi_{start} + \frac{k}{d^m}$. This power law like behavior is also observed in micropillar compression experiments [30].

To investigate the strain hardening of the martensite, simulations were carried out with a ξ_∞ (see Eq. (6)) value of either 1000 or 3000 MPa. Modifying this parameter alters the strain hardening of the martensite, but keeps the linear nature of the strain hardening of the martensite. This serves to examine the sensitivity of the presented approach with regard to the strain hardening of the martensite and to substantiate the aforementioned hypothesis on the effect of the parameters.

To underline the significance of a high-fidelity parameter set, a synthetic parameter set which produces the same macroscopic stress–strain curve as the calibrated was generated. A parameter set for ferrite from the literature by Liu et al. [59] was employed, and the martensite parameters were fitted based on the stress–strain curve of the DP800. Selected sRVE simulations with both parameter sets demonstrate the impact on the local stress and strain distribution.

3. Results

3.1. Strain hardening behavior of the polycrystalline ferrite in the dual phase sRVE

Table 1 presents the inversely calibrated parameters for the ferrite and the martensite. As outlined in the preceding section, the martensite parameters were solely estimated and will be discussed in greater detail in the parameter study in Section 3.3. The mean calibrated strain hardening, i.e. the change in the CRSS is illustrated in Fig. 5a as a solid orange line, alongside the experimental data (dashed black line), plotted against the mean shear strain. This is calculated by multiplying the global strain by a Taylor factor of 2.75, based on the pencil glide slip in *bcc* crystals ($\overline{T} = \overline{M\varepsilon}$) [12]. The orange crosses represent the grain-averaged ξ value of a single sRVE simulation, demonstrating the occurring scatter. The plot over the shear stress is used due to the comparability with Fig. 9b from Tian et al. [12]. It is evident that the modeling approach can be utilized to map the strain hardening, including its linear nature. In the range up to an average shear strain of 0.264, the strain hardening is almost perfectly matched with very little constant underestimation. In the subsequent range up to 0.402, the simulated slope is slightly lower than the experimentally measured slope. The slope of the mean strain hardening of the ferrite is 233 ± 9 MPa in the simulation, in comparison to 242 MPa in the experimental measurements. The standard deviation is calculated based on the minimal possible hardening and the maximum possible hardening. This represents a deviation of the mean strain hardening values of less than

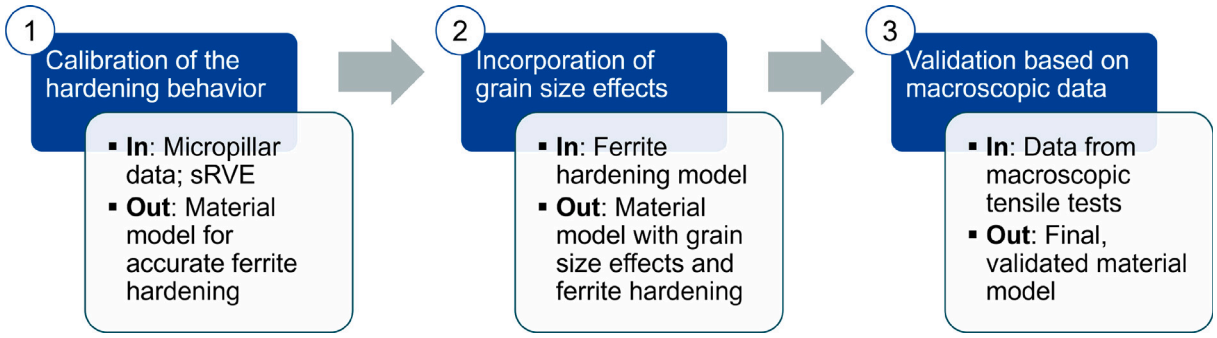

Fig. 4. Schematic workflow for the calibration scheme, consisting of the (1.) calibration of the hardening, (2.) the incorporation of the grain size effects and (3.) the final validation based on macroscopic data.

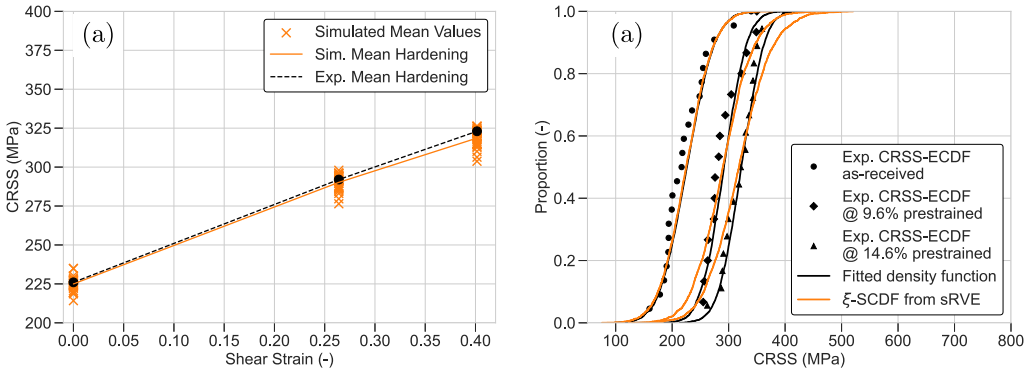

Fig. 5. Results for the strain hardening model. Comparison for mean CRSS vs ξ left, distributions right. (a) Mean ferrite hardening in sRVE compared to experimental data (black). Dashed line indicates the extrapolated mean, the crosses mark the mean ξ-values for the individual sRVE, (b) Comparison of CRSS-distributions (exp. vs. sim) at different (pre)-strain levels. Solid lines indicate the analytical CDFs, the dots the measured data. (For interpretation of the references to color in this figure legend, the reader is referred to the web version of this article.)

3.5%. Only three parameters (a, h_0 and ξ_∞) have to be fitted for the ferrite, with n being excluded from the fitting process since it controls the strain rate sensitivity, which is not needed in this study since all experiments and simulations being conducted under quasistatic conditions. ξ_0 is given from the distributions as stated before.

In Fig. 5b, the ECDF of the CRSS is compared to the ξ-SCDF, which is the density calculated based on every grain-averaged ξ-value in every simulation (orange curve). Each of the two simulative distributions consist of 3000 data points, 1000 ferrite grains in 10 sRVE x 3 simulations per sRVE. Overall, there is convincing agreement between simulations and experiments. However, the SCDFs are slightly broader, i.e. have a higher standard deviation, resulting in more very small or very large grain-averaged ξ values. In addition to the agreement at the different (pre)strain levels, the leftmost orange distribution demonstrates that the input distribution (black) is accurately represented by the distribution that has been reversely drawn from all the sRVE at a strain of 0.0. This underscores that the sample of 30 simulations is sufficient to capture the distribution of the CRSS and is therefore statistically representative.

Table 2 presents a summary of the results obtained from the strain hardening model and offers a comparison with the experimental data provided by Tian et al. [12], Table 2. The simulative standard deviation represented in the table is the average of all the individual sRVE standard deviations of ξ. Similar to the visual depiction in Fig. 5b, the greater width of the SCDF is evident in the form of the higher standard deviation at 0.096 and 0.146 (pre)strain. Compared to the experimental data, where the standard deviation of the ECDF decreases, there is an increase of the width of the density function in the simulation data. The contraction, i.e. the reduced standard deviation, is apparently not reflected in the strain hardening model.

Table 2
Results for the strain hardening model. The experimental values are taken from [12], table 2. ± denotes the standard error of the respective quantity.

Strain (%)	Mean (MPa)		Std (MPa)	
	Sim.	Exp.	Sim.	Exp.
0.0	225 ± 4	226 ± 9	37 ± 3	39 ± 2
9.6	290 ± 5	292 ± 8	46 ± 5	32 ± 4
14.6	319 ± 6	323 ± 11	50 ± 6	32 ± 2

3.2. Prediction of homogenized stress–strain curve using grain size scaling

The calibrated material parameters from Table 1 were coupled with algorithm 1 to include grain size effects on the CRSS in order to predict the macroscopic stress–strain curve. The grain size scaling yields a modified distribution of ξ_0 values. The estimated Hall–Petch parameters are τ_{start} = 77.84 MPa and k = 183.94 MPa, with a R^2-value of 0.88. No standard deviation is given for these parameters, as the fit of the Hall–Petch regression was only carried out using the three mean values of the CRSS.

Given that the grains in the sRVE are on average larger than 2 µm (3.76 µm ±3.04 µm), the center of mass of the density function is shifted to the left. However, the width of the function is also increased, since it is the product of two marginal distributions (grain size distribution and ξ_0-distribution). The mean value of ξ_0 shifts from 226 ± 40 MPa to 209 ± 53 MPa.

The true stress–strain curve from the sRVE-simulations, is depicted in Fig. 6 and is compared with the true stress–strain curve from the uniaxial tensile test. Since the stress–strain curves for the individual tensile tests are homogeneous, one representative experimental curve is depicted. The solid orange line delineates the mean value, while the

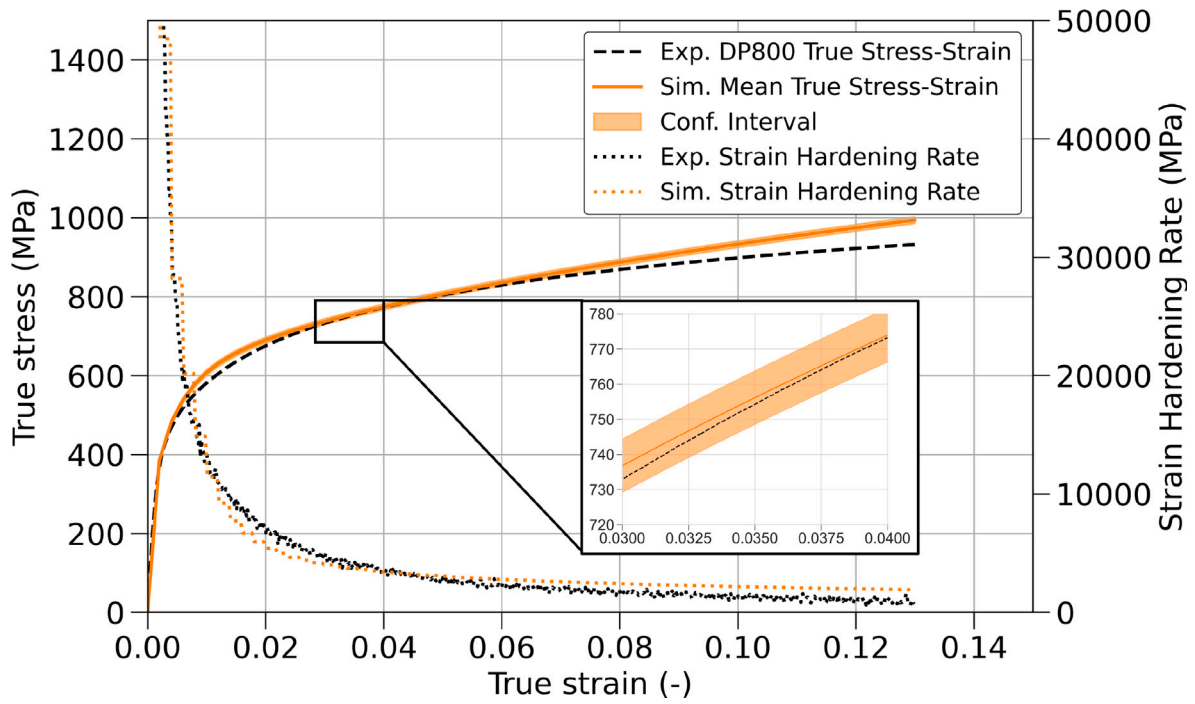

Fig. 6. Comparison of exp. true stress–strain curve with the sRVE-Simulations. The shaded area denotes the 95% confidence interval. The strain hardening rate denoted on the right y-axis.

shaded area represents the 95% confidence interval (see inset in Fig. 6). In order to enable the calculation of both quantities, the data points obtained from the simulations were piecewise linear interpolated, with the objective of establishing a comparison between the stresses at identical strain values across all curves, whether experimental or simulated. Given the considerable number of simulations conducted, the confidence interval is relatively narrow. Overall, there is good agreement between the simulated and experimental data. The simulations exhibit a slight tendency to overestimate the experimental stress level, particularly evident in the range of 0.005 to 0.015 and for strains higher then 0.07. For the rest of the value range, the experimental datapoints fall inside the confidence interval, underpinning that there is no statistically significant difference between the experimental data and the numerical prediction. The mean absolute error (MAE) was calculated between the experimental curve and the simulated mean value, yielding a value of 21±8 MPa, with ± denoting the averaged width of the shown confidence interval. The resulting mean absolute percentage error (MAPE) is 3.3%. It can be reasonably deduced that the major portion of the deviation are caused by the deviation at higher strains. For the regime up to 0.05 global strain, the error is only 12 ± 7 MPa (MAPE: 3.7%).

In addition to the high degree of agreement observed with regard to the stress–strain curve, there is also a high consistency between the numerically estimated and experimentally measured strain hardening rates (Fig. 6, right y-axis), which can be defined as the derivative of the stress–strain curve (in this example, more precisely, the numerical gradient of both curves). The favorable mapping of this important material parameter demonstrates that the mapping of the strain hardening in the ferrite (Fig. 5) also results in a favorable mapping of the homogenized strain hardening of the entire dual-phase sRVE. The good agreement of the curves also leads to a favorable agreement in yield strength. The $R_{p,0.2}$ measured in the uniaxial tensile test is 477 ± 10 MPa, whereas in the simulation, the value is 491 ± 22 MPa. The higher deviation is attributed to the greater scatter of the sRVE compared to the tensile test samples, which contain way more grains and martensite islands than a single sRVE.

3.3. Effect of the martensite strain hardening on the macroscopic stress–strain curve

The absence of a comparable calibration methodology for martensite is based on the assumption that the martensite strain hardening is insignificant with respect to the stress–strain response of the bulk material due to the significant phase contrast. To test the validity of this assumption, two additional synthetic stress–strain curves and corresponding material parameter sets were generated for the martensite. The first set was constructed with ξ_∞ = 1000 MPa, which reduces the strain hardening to almost 0 and leads to a yield-to-tensile stress ratio of approximately 1.0. The second curve was generated with ξ_∞ = 3000 MPa, which results in a more pronounced strain hardening then the base set with ξ_∞ = 2000 MPa. It should be noted that the modifications only affect the strain hardening, with the yield point remaining at a constant value of approximately 3000 MPa, which was determined by Tian et al. using micropillar compression experiments in the bulk regime [52]. Fig. 7a depicts the three resulting stress–strain curves. It is evident that the curves exhibit a significant degree of divergence from one another for strains up to 0.14. With ξ_∞ = 1000 MPa, a stress value at 0.14 global strain $\sigma_{0.14}$ = 3046 MPa is achieved, which is very close to the yield strength. For ξ_∞ = 2000 MPa this is 3604 MPa, and with ξ_∞ = 3000 MPa 4360 MPa.

All 30 sRVE simulations were replicated with the revised martensite material parameters. The extensive number of simulations was primarily employed to quantify the scatter resulting from local fluctuations in the ferrite based on the statistical nature of the material parameters. Fig. 7b illustrates the resulting true stress–strain curves averaged over all 30 simulations with the varying stress–strain curves for the martensite. For the sake of simplicity, the experimental stress–strain curve was not included. Substantial discrepancies between the three curves emerge only at strains exceeding approximately 0.06. While a divergence is noticeable at higher elongations, it is minimal in comparison to the pronounced variations in the stress–strain curves for the single-phase martensite. This phenomenon can be attributed to the fact that martensite exhibits predominantly elastic deformation, with very little plastic deformation. Table 3 shows the number of grid points

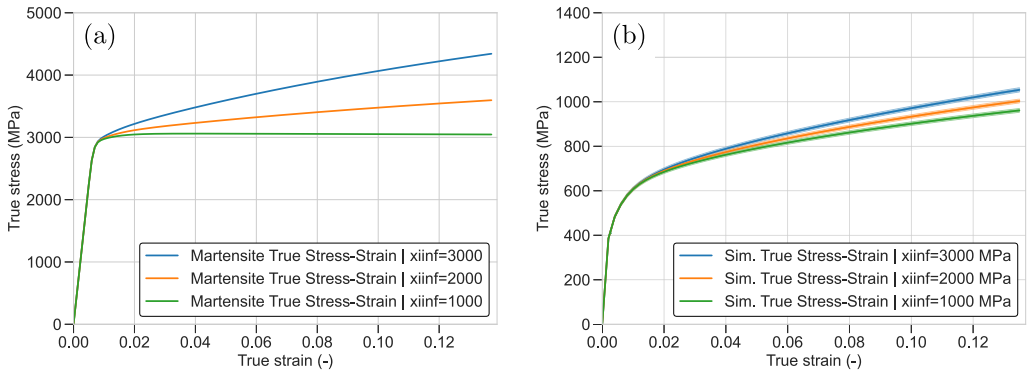

Fig. 7. Results for parameter study on the martensite hardening. (a) Three different stress–strain curves for the martensite phase (ξ_∞ = 3000 MPa, ξ_∞ = 2000 MPa, ξ_∞ = 1000 MPa). Yield strength stays constant, only the hardening changes, (b) Aggregated stress–strain curves with ξ_∞ = 3000 MPa, ξ_∞ = 2000 MPa, ξ_∞ = 1000 MPa. Shaded area shows the confidence interval averaged over 30 simulations.

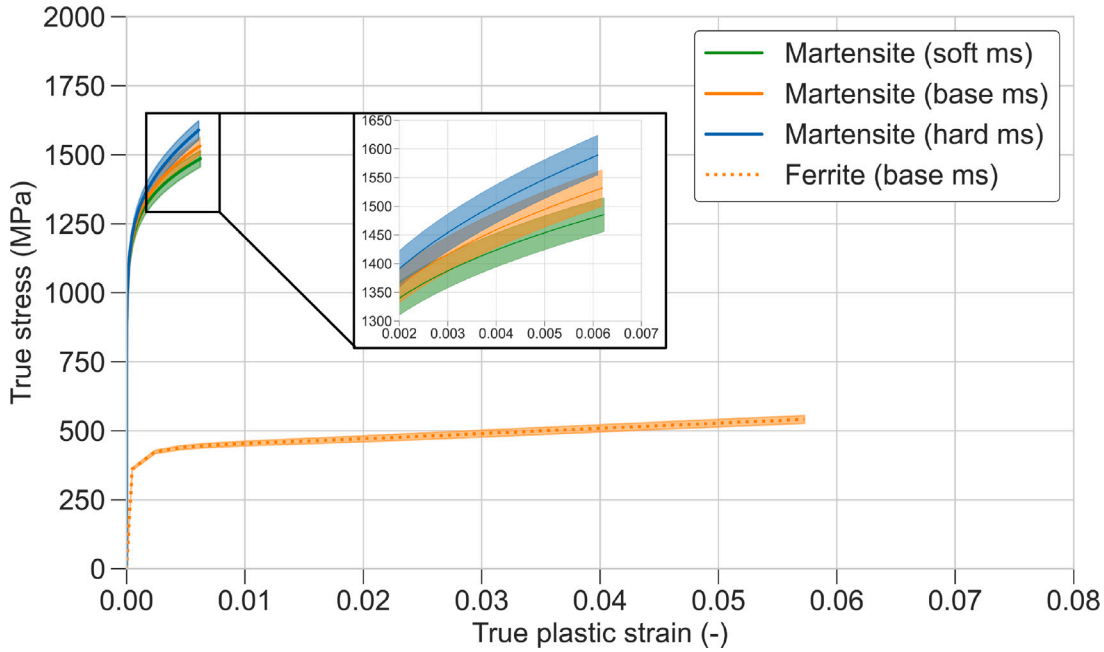

Fig. 8. Individual stress–strain curves extracted from the dualphase sRVE for different strength martensite, aggregated over all sRVEs. In orange, dashed, the curve of the ferrite is shown as a comparison. (For interpretation of the references to color in this figure legend, the reader is referred to the web version of this article.)

Table 3
Fraction of martensite grid points exceeding the yield strength of 3000 MPa at a homogenized global strain of 0.05, depending on the martensite strain hardening.

Parameter set	Fraction of martensite grid points exceeding the yield strength (–)
$\xi_\infty = 1000$	0.05 ± 0.015
$\xi_\infty = 2000$	0.06 ± 0.019
$\xi_\infty = 3000$	0.08 ± 0.024

of the martensite phase which exhibit plastic deformation, i.e. having a stress exceeding the yield strength of 3000 MPa. The grid points were averaged over all 30 sRVE simulations. It is evident that a negligible proportion of elements undergo plastic deformation (less than 10%), thereby rendering the hardening of the flow curve solely significant for these specific points.

The significant phase contrast between martensite and ferrite, as illustrated in Fig. 8, is predominantly accountable for this deformation behavior. The stress–strain curves for the martensite and ferrite are displayed here, aggregated over all sRVE simulations and for all three distinct martensite curves. The global strain of each sRVE is 0.05. For the sake of simplicity, a single ferrite curve is incorporated. The distinction between martensite and ferrite is evident, with ferrite exhibiting strain values that are more than six times higher than those observed in martensite. The three distinct martensite curves exhibit minimal deviation, and the mean stress of the martensite is distinctly lower than the martensite's yield point for all three different martensite strength levels.

The results demonstrate that the varying stress–strain curves of martensite exert a similar, albeit modest, impact on the macroscopic stress–strain curve and the martensite stress–strain curves in the sRVE. This implies that due to the considerable divergence in strength between the two phases, the hardening of the martensite exerts a negligible influence on the strain partitioning.

3.4. Effect of the size scaling exponent m on the macroscopic stress–strain curve

Subsequent to the investigation of the influence of martensite hardening, an analysis was conducted on the influence of the size scaling exponent m. The true stress–strain curves of the simulations with m = 0.3 and m = 0.7 are presented in Fig. 9a. The base curve (Fig. 6) can

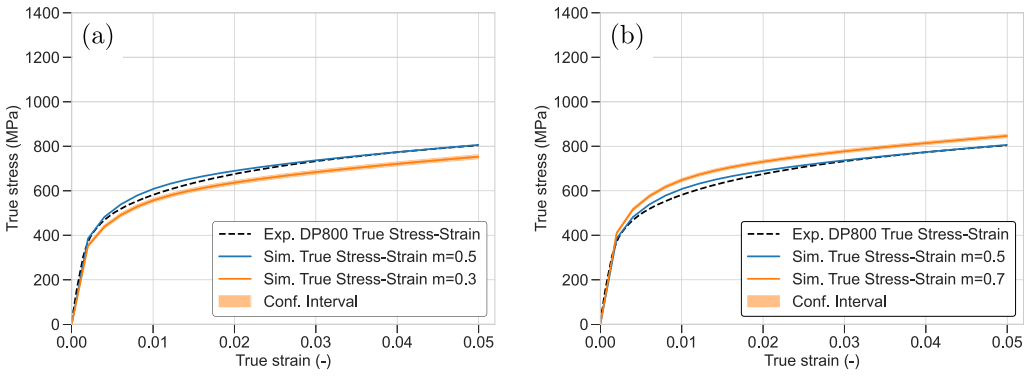

Fig. 9. Results for the parameter study on the size scaling exponent m. (a) Aggregated flowcurves with $m = 0.3$. Solid blue line shows the mean value with $m = 0.5$, which corresponds to the classical Hall–Petch-assumption, (b) Aggregated flowcurves with $m = 0.7$. Solid blue line shows the mean value with $m = 0.5$, which corresponds to the classical Hall–Petch-assumption. (For interpretation of the references to color in this figure legend, the reader is referred to the web version of this article.)

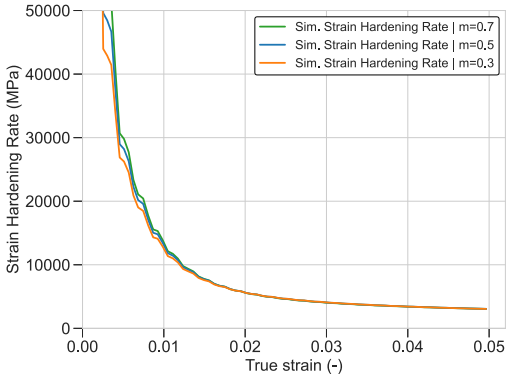

Fig. 10. Comparison of the strain hardening rates for different size scaling exponents m. The experimental slope was omitted due to better visibility.

be seen as a solid blue line, corresponding to $m = 0.5$. Again, all 30 simulations were repeated using the different m-values for the grain size scaling. Since the size scaling exponents directly affects the ferrite, the effect has to be investigated using all 30 sRVE-sample.

The different size scaling exponents lead to a modified Hall–Petch regression. For $m = 0.3$, we have $\tau_{start} = -19.45$ MPa and $k = 281.29$ MPa, for $m = 0.7$ $\tau_{start} = 119.15$ and $k = 142.52$ MPa. Although a negative value for τ_{start} is physically impossible, simulations were nevertheless conducted for the sake of completeness. In contrast to the influence of the hardening of the martensite, the influence of the size scaling exponent and the modified size scaling on the bulk stress–strain response is markedly pronounced, with $m = 0.3$ resulting in an underestimation of the entire curve and $m = 0.7$ leading to an overestimation. The corresponding MAE is 46.6 ± 6.7 MPa for $m = 0.3$ and 41.4 ± 8.2 MPa for $m = 0.7$, more than 4x the MAE compared to $m = 0.5$. The discrepancy in the stress–strain curve can be attributed to the alteration in the slope of the Hall–Petch regression, which in turn affects the degree to which grain size exerts an influence. A decrease in m results in a greater slope, which in turn leads to an underestimation of the stress–strain curve due to a stronger consideration of the grain size. Conversely, an increase in m has the opposite effect.

Fig. 10 depicts the mean strain hardening rates for all three sets of simulations. Only in regions of very low strain ($\varepsilon \leq 0.01$) there is a visible difference, whereupon the curves become almost identical. This demonstrates that the size scaling exponent, m, exerts an influence solely on the level of the stress–strain curve, with nearly no impact on strain hardening. Consequently, from a phenomenological perspective, m acts as some kind of scaling factor on the overall stress level.

3.5. Case study: Influence of different parameter sets on the stress and strain partitioning

To illustrate the significance of accurate material parameters, a parameter study was conducted using two sets of parameters with distinct characteristics. For the sake of simplicity, only a single sRVE was selected for this case study. Fig. 11 depicts the numerically predicted stress–strain curves in conjunction with the experimental ones, alongside the stress–strain curves for the individual phases. Both parameter sets replicate the homogenized macroscopic behavior well and exhibit comparable MAE of 9 MPa (set 1) and 10 MPa (set 2). As this is merely a single simulation, there is no confidence interval for either MAE value. In set 1, characterized by a high phase contrast, the ferrite carries the majority of the applied deformation, resulting in an average strain in the ferrite that is more than twice as high as for the martensite and a large difference in the final stress. In set 2, both phases exhibit comparable strength, leading to a markedly more homogeneous deformation and a notable reduction in the deviation in the stress values.

The distinction is also apparent at the local level within the sRVE, as illustrated in Fig. 12. This figure illustrates an exemplary slice through the sRVE, wherein the von-Mises equivalent plastic strain (PEEQ) is visible in the upper row. Set 1 is illustrated on the left, and set 2 is illustrated on the right. While the magnitude of the plastic strain differs between the two sets (please note that the colorbars are different for the sake of comparability), a strain localization can be observed at the same location (red circle) within a ferrite grain, encapsulated between two martensite islands. However, an examination of the principle stress (σ_1) reveals a markedly different distribution between the sets. In set one, there is a pronounced stress localization with stress values reaching around 5000 MPa at the narrowest point of a larger martensitic structure (white circle, left), which extends over half the width of the section through the sRVE. In contrast, no stress localization can be identified at the same location (white circle, right) for parameter set 2. In this set, the stress hotspots are at different position in the sRVE. This indicates that this material model predicts the stress localization at completely different points in the microstructure, which will likely lead to a different prediction of the damage initiation hotspots. This underlines the importance of a correct prediction of the stress–strain curves of the individual phase with high-fidelity model parameters.

4. Discussion

The objective of the discussion is to gain insight into the advantages and limitations of the proposed approach for calibrating CP model parameters. Furthermore, the impact of diverse influencing variables and the implications on microstructural modeling on small scales is discussed.

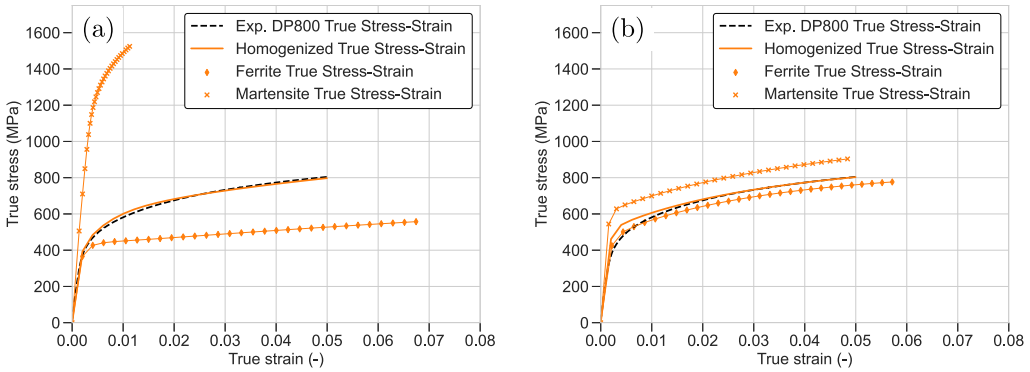

Fig. 11. Global stress–strain curves and stress–strain partitioning for two different parameter sets. (a) Exemplary stress–strain comparison and partitioning for a single sRVE using the calibrated parameter set (Set 1), (b) Exemplary stress–strain comparison and partitioning for a single sRVE using an artificial parameter set (Set 2).

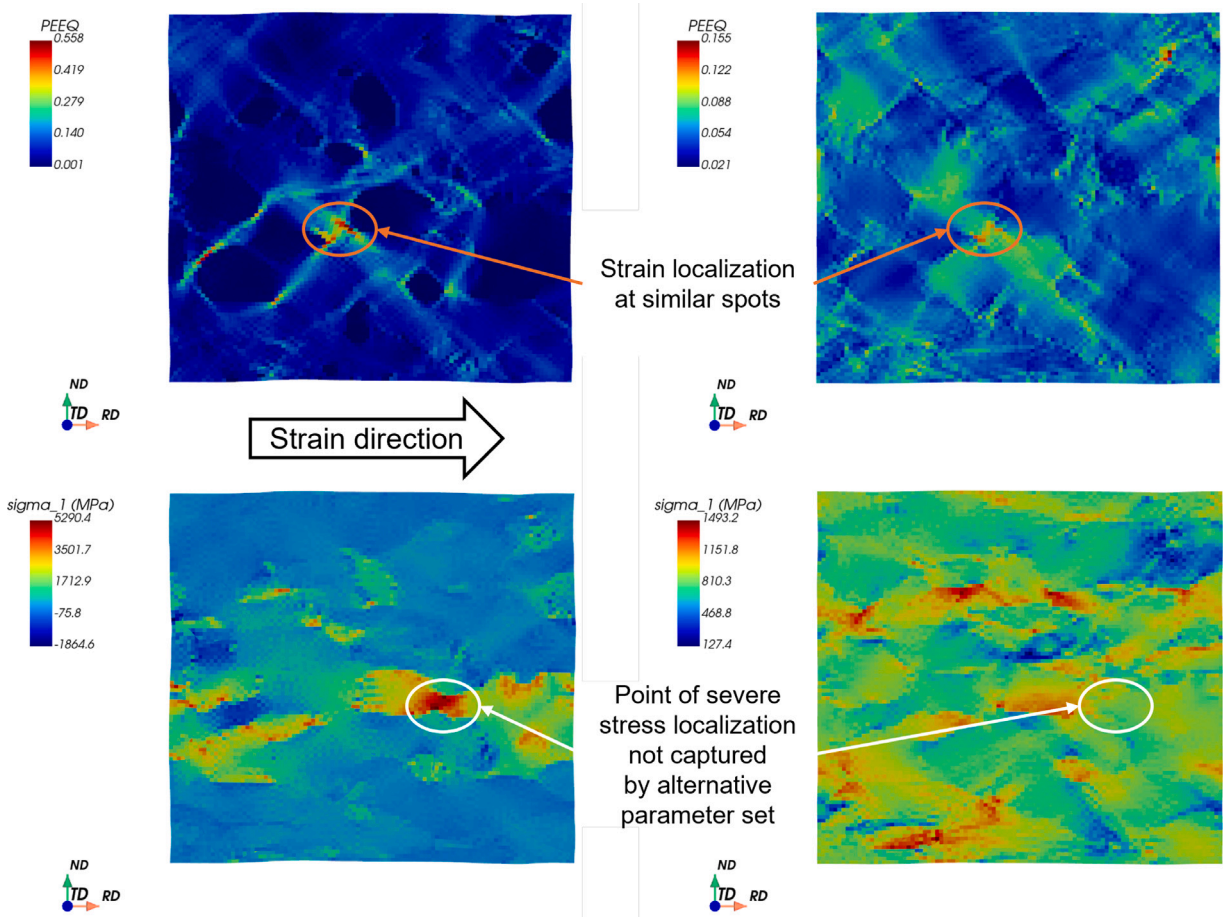

Fig. 12. Plastic strain and principle stress localization for two different material models in a slice through an exemplary sRVE. The left column corresponds to the model from this study, the right one to a synthetic model with an artificially lowered phase contrast.

4.1. Comparison with other calibration approaches

In comparison to alternative techniques for CP parameter identification, the key benefit of the proposed methodology is the ability to obtain quasi-unique parameter sets through the incorporation of a diverse set of data from the microscale. In contrast, Sedighiani et al. [16] demonstrated that calibration via macroscopic tensile testing frequently yields non-unique results for most of the model parameters. It can be stated that the model parameters from the proposed approach are much more unambiguous than parameters obtained by simple uniaxial tensile tests, since both the distributions of the CRSS and the mean strain hardening are incorporated as target functions. For example, the linear nature of the ferrite strain hardening model at very low strains is only displayable with a low value for the initial hardening h_0 and cannot be obtained otherwise. To quantify the reduction in uncertainty for the approach presented, many parameter sets could be generated and compared using computer-aided optimization techniques, such as genetic algorithms [16] or Bayesian optimization [60]. Given the considerable number of simulations that would be required, this was not included in the study. In comparison with other approaches for calibration, which involve nanoindentation and a subsequent fit of the second phase based on tensile test results, the macroscopic stress–strain curve can be excluded from the calibration process in the approach presented here. In addition, with these different approaches, there

is always the possibility that an error in the calibration of the first phase will be compensated by a subsequent error in the second phase calibration and will still result in a good macroscopic stress–strain curve despite a wrong stress–strain partitioning. As shown in Section 3.5, Fig. 12, this quickly leads to a clearly erroneous prediction of local material properties. As shown in Gallardo-Basile et al. [25], the calibration with nanoindentations is complex and quickly leads to an overestimation of the macroscopic material behavior without exact consideration of the boundary conditions or additional data such as micropillar compression. It should be noted that during nanoindentaton, a complex stress state with steep gradients is present. The interaction of the plastic zone size of the indent with neighboring grains and interfaces is another challenge. To the best of our knowledge, most nanoindentation based approaches have not been validated for a two-phase material on the macroscale. As mentioned in the introduction, calibration of the strain hardening directly from the micropillar stress–strain curve is not possible due to the free surfaces of the micropillar and the fact that the apparent strain hardening does not represent the strain hardening of a material [6,12].

4.2. Mapping properties from the micro- to the macroscale

The findings of Section 3 show that the homogenized macroscopic stress–strain curve can be accurately predicted by the developed calibration approach, even in the absence of data from macroscopic tests. The slight overestimation of the stress–strain curve in the low strain regime (around 0.01 - 0.015) may be attributed to the presence of residual compressive stress within the ferrite phase, which is a consequence of the phase transformation that occurs during the intercritical annealing and subsequent quenching [61]. Khadkhodapour et al. [62] were able to determine the varying hardness of the ferrite grains in accordance with their distance from the martensite, which was attributed to a heterogeneous dislocation structure caused by the martensitic transformation. Therefore, a ferrite grain cannot be regarded as homogeneous but rather exhibits a certain degree of inhomogeneity. However, the induced residual stresses are presumably already depleted at relatively low global strains and, therefore, this effect can be regarded as negligible at higher plastic strain values. For the overestimation of the experimental curve for strains higher then 0.07, one possible explanation is the nature of the CP-model, which renders the simulated stress–strain curve linear from relatively low strains on. In addition, no effects like for example damage-induced softening are included in the model. Another influencing factor is the hardening of the martensite, which will be discussed later.

The scaling of the CRSS of individual grains based on the sample size effect observed in the *in situ* micropillar compression experiments is critical for the correct transfer of properties from the micro to the macroscale. Since no separate size scaling law was derived in Tian et al. [52] due to the limited pillar diameter variations, the assumption of $m = 0.5$ from the Hall–Petch equation was used. The size effects in these small-volume compression tests can often be described by a power law $\sigma_y \sim w^{-m}$ like the Hall–Petch relationship [63]. The effect of the size scaling exponent on the macroscopic stress–strain data is very pronounced, as can be seen for the simulations conducted for $m = 0.3$ and $m = 0.7$, however, m only influences the overall level of the curve, the strain hardening remains unaffected (see strain hardening rates in Fig. 9). Therefore, the specific choice of m is not critical for the correct mapping of the strain hardening using the presented approach.

Many values for m can be found in the literature, ranging from 0.22 up to 1 [64,65]. Kraft et al. [66] were able to show, however, that there is no uniform, material-specific size scaling exponent, but that m varies for different sample size d ranges. They defined three distinct regimes with different underlying mechanisms: Regime III (“bulk-like”) starts from around $d > 1$ μm and therefore covers the micropillar used in this work. According to Kraft et al. [66], $m = 0.5$ can be assumed for this regime, which is why this was also used in this study. For a real validation, however, an individual m would have to be derived, for which further micropillars of different sizes are necessary.

4.3. Influence of the martensite strain hardening behavior

The experimental data from the micropillar compression tests from Tian et al. [12] do not show pronounced apparent strain hardening, however, pillar compression is not well-suited to measure the strain hardening [6]. To model the possible impact of strain hardening behavior of martensite, two assumptions were made. Firstly, it was assumed that due to the considerable number of interfaces present in the martensite pillars, the properties are analogous to those of the martensite, without size effects. Consequently, both the yield strength and strain hardening are deemed to be transferable. The results of both the calibration and the parameter study on the martensite hardening (Fig. 10) indicate that the yield strength is transferable, and that size effect does not appear to be a significant factor. The second assumption, that the strain hardening of the martensite plays a secondary role in the overall material’s strain hardening, due to the significant phase contrast, is also underpinned by the parameter study (see Fig. 8). Visible deviations in the predicted stress–strain curve are observable only from larger strains of 0.06–0.07 or more, with a variation in the strain hardening parameters of the martensite. In addition, the martensite deforms almost exclusively elastically, more than 90% of the elements remain below the yield strength of 3000 MPa at a global strain of 0.05 (see Table 2), only minimally influenced by the hardening of the martensite. Nevertheless, the strain hardening of the martensite is undoubtedly a crucial factor in enhancing the prediction quality at elevated strains. When strains are high globally, the deformation at the local level no longer occurs almost exclusively in the ferrite; rather, the martensite must also carry part of the applied deformation. In conclusion, the findings indicate that an exact characterization of the martensite may be dispensable under specific boundary conditions. Furthermore, the hardening of the martensite could be calibrated inversely using the data from the macroscopic tensile test, but then these results would only be available as validation data to a limited extent. However, if the second phase is markedly softer than the present martensite, the approach may be inadequate. In such a scenario, it may be necessary to calibrate both phases using micropillar compression on prestrained samples.

It is also important to note that the martensite considered in this analysis exhibits significantly higher strength than the ferrite phase. Consequently, the global homogenized stress–strain curve does not follow a “rule of mixture”-like principle based on the phase fractions. For the present material, a similar approach would likely result in an overestimation of the macroscopic stress–strain curve by a factor of x2 - x3, or alternatively, an estimation of the martensite to be significantly softer than its actual mechanical properties. Likely, the high phase contrast alters the local deformation and stress partitioning within the virtual microstructure in a manner that renders the “Rule of Mixture” inapplicable.

4.4. Implications on damage behavior and modeling

Although high-fidelity information on strain hardening and flow behavior do not directly correspond to the damage behavior of the material, it is a first step towards understanding the damage behavior of a material. Further material parameters such as the fracture toughness of individual phases [67–69] are required for a true modeling of the initiation and especially the evolution of ductile damage. For instance, the fracture toughness of individual phases can be determined through the implementation of microscopic fracture mechanics tests. However, the transfer of the fracture mechanics parameters into a numerical model is not trivial due to the crack assumptions required in the general concepts of fracture mechanics.

As shown by Yan et al. [9] damage is a phenomenon that is highly dependent on local heterogeneities caused by microstructure and material properties, which is why a correct prediction of the macroscopic stress–strain curve is insufficient to predict damage. In

particular, the locally massively different stress distribution observed in Fig. 12 underlines the importance of a realistic calibration of the mechanical behavior of all phases, as performed in this work. Since the maximum principal stress acts as the driving force for crack initiation and propagation, it is a good indicator of the damage behavior of the material. In contrast to that, the strain distribution is at least qualitatively similarly predicted by both considered parameter sets. This is important because the strain distribution can be determined using e.g. μDIC [70], even though these measurements are inherently 2D. However, the stress distribution cannot be measured in a comparable way.

5. Conclusion

The objective of this study was to develop a novel methodology for calibrating crystal plasticity models using micropillar compression experiments. This approach was specifically designed to identify material parameters that accurately predict local heterogeneity caused by the phase contrast and strain hardening in multi-phase materials and, consequently, damage behavior. To achieve this, we employed sRVE and crystal plasticity simulations. Based on the findings, we can draw the following conclusions:

1. The parameters of a crystal plasticity model were successfully calibrated and validated using the macroscopic stress–strain curve. Size effects could also be derived from the micropillar tests and successfully transferred to the grains in the RVE.
2. The hardening of the martensite only shows an influence at higher strains and can therefore be neglected.
3. The effect of the assumed size-scaling exponent on the level of the stress–strain curve of the bulk is much more pronounced. The assumption of $m = 0.5$ similar to the Hall–Petch relation could be validated.
4. In summary, the calibrated parameters can predict the phase contrast between hard and soft phase at any global strain, as the initial phase contrast and the strain hardening of the ferrite are correctly modeled. This is the first step of accurately modeling damage initiation and evolution in subsequent studies.
5. This admittedly very complex approach can also be used to determine the macroscopic stress vs strain behavior if (a) the material volume to be tested does not allow for standardized samples or (b) if it is not possible to remove more material from a structure to be examined

To further develop the approach, the quantification of the uniqueness of the calibrated parameters should be addressed by means of computer-aided optimization. This can ensure even better comparability with other approaches.

CRediT authorship contribution statement

Niklas C. Fehlemann: Writing – original draft, Investigation, Methodology, Software, Conceptualization. **Angelica Medina:** Resources, Writing – review & editing, Data curation, Formal analysis. **Subin Lee:** Resources, Writing – review & editing, Formal analysis. **Christoph Kirchlechner:** Resources, Supervision, Writing – review & editing, Funding acquisition. **Sebastian Münstermann:** Writing – review & editing, Funding acquisition, Project administration, Supervision.

Declaration of competing interest

The authors declare that they have no known competing financial interests or personal relationships that could have appeared to influence the work reported in this paper.

Acknowledgments

This research was funded by the Deutsche Forschungsgemeinschaft (DFG, German Research Foundation), Germany, Projektnummer 278868966, TRR 188, Project B03 and B05. The simulations were carried out with computing resources granted by RWTH Aachen University, Germany under project rwth1645. CK and SL acknowledge financial support from the Robert Bosch foundation, Germany.

Data availability

The numerical data will be made available on request and will later be published at the IBF-MM github-page: https://github.com/ibf-RWTH.

References

[1] A. Schowtjak, J. Gerlach, W. Muhammad, A.P. Brahme, T. Clausmeyer, K. Inal, A.E. Tekkaya, Prediction of ductile damage evolution based on experimental data using artificial neural networks, Int. J. Solids Struct. 257 (2022) 111950, http://dx.doi.org/10.1016/j.ijsolstr.2022.111950.
[2] A. Schowtjak, R. Schulte, T. Clausmeyer, R. Ostwald, A.E. Tekkaya, A. Menzel, ADAPT — A diversely applicable parameter identification tool: Overview and full-field application examples, Int. J. Mech. Sci. 213 (2022) 106840, http://dx.doi.org/10.1016/j.ijmecsci.2021.106840.
[3] M. Rossi, A. Lattanzi, L. Morichelli, J.M.P. Martins, S. Thuillier, A. Andrade-Campos, S. Coppieters, Testing methodologies for the calibration of advanced plasticity models for sheet metals: A review, Strain 58 (6) (2022) http://dx.doi.org/10.1111/str.12426.
[4] A. Koester, A. Ma, A. Hartmaier, Atomistically informed crystal plasticity model for body-centered cubic iron, Acta Mater. 60 (9) (2012) 3894–3901, http://dx.doi.org/10.1016/j.actamat.2012.03.053.
[5] F. Roters, P. Eisenlohr, T.R. Bieler, D. Raabe, Crystal Plasticity Finite Element Methods: In Materials Science and Engineering, first ed, Wiley-VCH, Weinheim, 2010.
[6] G. Dehm, B.N. Jaya, R. Raghavan, C. Kirchlechner, Overview on micro- and nanomechanical testing: New insights in interface plasticity and fracture at small length scales, Acta Mater. 142 (2018) 248–282, http://dx.doi.org/10.1016/j.actamat.2017.06.019.
[7] R. Maaß, P.M. Derlet, Micro-plasticity and recent insights from intermittent and small-scale plasticity, Acta Mater. 143 (2018) 338–363, http://dx.doi.org/10.1016/j.actamat.2017.06.023.
[8] H. Ghassemi-Armaki, R. Maaß, S.P. Bhat, S. Sriram, J.R. Greer, K.S. Kumar, Deformation response of ferrite and martensite in a dual-phase steel, Acta Mater. 62 (2014) 197–211, http://dx.doi.org/10.1016/j.actamat.2013.10.001.
[9] D. Yan, C.C. Tasan, D. Raabe, High resolution in situ mapping of microstrain and microstructure evolution reveals damage resistance criteria in dual phase steels, Acta Mater. 96 (2015) 399–409, http://dx.doi.org/10.1016/j.actamat.2015.05.038.
[10] J. Kadkhodapour, S. Schmauder, D. Raabe, S. Ziaei-Rad, U. Weber, M. Calcagnotto, Experimental and numerical study on geometrically necessary dislocations and non-homogeneous mechanical properties of the ferrite phase in dual phase steels, Acta Mater. 59 (11) (2011) 4387–4394, http://dx.doi.org/10.1016/j.actamat.2011.03.062.
[11] C.C. Tasan, M. Diehl, D. Yan, C. Zambaldi, P. Shanthraj, F. Roters, D. Raabe, Integrated experimental–simulation analysis of stress and strain partitioning in multiphase alloys, Acta Mater. 81 (2014) 386–400, http://dx.doi.org/10.1016/j.actamat.2014.07.071.
[12] C. Tian, C.F. Kusche, A. Medina, S. Lee, M.A. Wollenweber, R. Pippan, S. Korte-Kerzel, C. Kirchlechner, Understanding the damage initiation and growth mechanisms of two DP800 dual phase grades, Mater. Des. 238 (2024) 112630, http://dx.doi.org/10.1016/j.matdes.2024.112630.
[13] T. de Geus, F. Maresca, R. Peerlings, M. Geers, Microscopic plasticity and damage in two-phase steels: On the competing role of crystallography and phase contrast, Mech. Mater. 101 (2016) 147–159, http://dx.doi.org/10.1016/j.mechmat.2016.07.014.
[14] S. Bargmann, B. Klusemann, J. Markmann, J.E. Schnabel, K. Schneider, C. Soyarslan, J. Wilmers, Generation of 3D representative volume elements for heterogeneous materials: A review, Prog. Mater. Sci. 96 (2018) 322–384, http://dx.doi.org/10.1016/j.pmatsci.2018.02.003.
[15] Y.-z. Wang, S.-l. Zang, L. Sun, J.-w. Ma, Constructing micro-mechanical representative volume element of medium Mn steel from EBSD data, Mater. Des. 129 (2017) 34–43, http://dx.doi.org/10.1016/j.matdes.2017.04.100.
[16] K. Sedighiani, M. Diehl, K. Traka, F. Roters, J. Sietsma, D. Raabe, An efficient and robust approach to determine material parameters of crystal plasticity constitutive laws from macro-scale stress–strain curves, Int. J. Plast. 134 (2020) 102779, http://dx.doi.org/10.1016/j.ijplas.2020.102779.

[17] V. Herrera-Solaz, J. LLorca, E. Dogan, I. Karaman, J. Segurado, An inverse optimization strategy to determine single crystal mechanical behavior from polycrystal tests: Application to AZ31 Mg alloy, Int. J. Plast. 57 (2014) 1–15, http://dx.doi.org/10.1016/j.ijplas.2014.02.001.

[18] C. Miehe, J. Schröder, J. Schotte, Computational homogenization analysis in finite plasticity simulation of texture development in polycrystalline materials, Comput. Methods Appl. Mech. Engrg. 171 (3–4) (1999) 387–418, http://dx.doi.org/10.1016/S0045-7825(98)00218-7.

[19] H. Wang, B. Raeisinia, P.D. Wu, S.R. Agnew, C.N. Tomé, Evaluation of self-consistent polycrystal plasticity models for magnesium alloy AZ31B sheet, Int. J. Solids Struct. 47 (21) (2010) 2905–2917, http://dx.doi.org/10.1016/j.ijsolstr.2010.06.016.

[20] K. Sedighiani, K. Traka, F. Roters, D. Raabe, J. Sietsma, M. Diehl, Determination and analysis of the constitutive parameters of temperature-dependent dislocation-density-based crystal plasticity models, Mech. Mater. 164 (2022) 104117, http://dx.doi.org/10.1016/j.mechmat.2021.104117.

[21] A. Leitner, V. Maier-Kiener, D. Kiener, Essential refinements of spherical nanoindentation protocols for the reliable determination of mechanical flow curves, Mater. Des. 146 (2018) 69–80, http://dx.doi.org/10.1016/j.matdes.2018.03.003.

[22] C. Zambaldi, Y. Yang, T.R. Bieler, D. Raabe, Orientation informed nanoindentation of a-titanium: Indentation pileup in hexagonal metals deforming by prismatic slip, J. Mater. Res. 27 (1) (2012) 356–367, http://dx.doi.org/10.1557/jmr.2011.334.

[23] C.C. Tasan, J. Hoefnagels, M. Diehl, D. Yan, F. Roters, D. Raabe, Strain localization and damage in dual phase steels investigated by coupled in-situ deformation experiments and crystal plasticity simulations, Int. J. Plast. 63 (2014) 198–210, http://dx.doi.org/10.1016/j.ijplas.2014.06.004.

[24] A. Chakraborty, P. Eisenlohr, Evaluation of an inverse methodology for estimating constitutive parameters in face-centered cubic materials from single crystal indentations, Eur. J. Mech. A Solids 66 (2017) 114–124, http://dx.doi.org/10.1016/j.euromechsol.2017.06.012.

[25] F.-J. Gallardo-Basile, F. Roters, R.M. Jentner, J.P. Best, C. Kirchlechner, K. Srivastava, S. Scholl, M. Diehl, Application of a nanoindentation-based approach for parameter identification to a crystal plasticity model for bcc metals, Mater. Sci. Eng.: A 881 (2023) 145373, http://dx.doi.org/10.1016/j.msea.2023.145373.

[26] R.-M. Rodriguez, I. Gutiérrez, Unified formulation to predict the tensile curves of steels with different microstructures, Mater. Sci. Forum 426–432 (2003) 4525–4530, http://dx.doi.org/10.4028/www.scientific.net/MSF.426-432.4525.

[27] L. Samek, B.C. de Cooman, J. van Slycken, P. Verleysen, J. Degrieck, Physical metallurgy of multi–phase steel for improved passenger car crash–worthiness, Steel Res. Int. 75 (11) (2004) 716–723, http://dx.doi.org/10.1002/srin.200405833.

[28] N. Vajragupta, P. Wechsuwanmanee, J. Lian, M. Sharaf, S. Münstermann, A. Ma, A. Hartmaier, W. Bleck, The modeling scheme to evaluate the influence of microstructure features on microcrack formation of DP-steel: The artificial microstructure model and its application to predict the strain hardening behavior, Comput. Mater. Sci. 94 (2014) 198–213, http://dx.doi.org/10.1016/j.commatsci.2014.04.011.

[29] H. Ghassemi-Armaki, P. Chen, S. Bhat, S. Sadagopan, S. Kumar, A. Bower, Microscale-calibrated modeling of the deformation response of low-carbon martensite, Acta Mater. 61 (10) (2013) 3640–3652, http://dx.doi.org/10.1016/j.actamat.2013.02.051.

[30] J.R. Greer, W.C. Oliver, W.D. Nix, Size dependence of mechanical properties of gold at the micron scale in the absence of strain gradients, Acta Mater. 53 (6) (2005) 1821–1830, http://dx.doi.org/10.1016/j.actamat.2004.12.031.

[31] M.F. Horstemeyer, M.I. Baskes, S.J. Plimpton, Length scale and time scale effects on the plastic flow of fcc metals, Acta Mater. 49 (20) (2001) 4363–4374, http://dx.doi.org/10.1016/S1359-6454(01)00149-5.

[32] C. Motz, D. Weygand, J. Senger, P. Gumbsch, Initial dislocation structures in 3-D discrete dislocation dynamics and their influence on microscale plasticity, Acta Mater. 57 (6) (2009) 1744–1754, http://dx.doi.org/10.1016/j.actamat.2008.12.020.

[33] D. Weygand, L.H. Friedman, E. van der Giessen, A. Needleman, Aspects of boundary-value problem solutions with three-dimensional dislocation dynamics, Modelling Simul. Mater. Sci. Eng. 10 (4) (2002) 437–468, http://dx.doi.org/10.1088/0965-0393/10/4/306.

[34] E.O. Hall, The deformation and ageing of mild steel: III discussion of results, Proc. Phys. Soc. Sect. B 64 (9) (1951) 747–753, http://dx.doi.org/10.1088/0370-1301/64/9/303.

[35] N.J. Petch, The cleavage strength of polycrystals, 1953.

[36] P. van Beers, G.J. McShane, V.G. Kouznetsova, M. Geers, Grain boundary interface mechanics in strain gradient crystal plasticity, J. Mech. Phys. Solids 61 (12) (2013) 2659–2679, http://dx.doi.org/10.1016/j.jmps.2013.08.011.

[37] L.P. Evers, D.M. Parks, W. Brekelmans, M. Geers, Crystal plasticity model with enhanced hardening by geometrically necessary dislocation accumulation, J. Mech. Phys. Solids 50 (11) (2002) 2403–2424, http://dx.doi.org/10.1016/S0022-5096(02)00032-7.

[38] E. Bittencourt, Interpretation of the size effects in micropillar compression by a strain gradient crystal plasticity theory, Int. J. Plast. 116 (2019) 280–296, http://dx.doi.org/10.1016/j.ijplas.2019.01.011.

[39] P. Lin, Z. Liu, Z. Zhuang, Numerical study of the size-dependent deformation morphology in micropillar compressions by a dislocation-based crystal plasticity model, Int. J. Plast. 87 (2016) 32–47, http://dx.doi.org/10.1016/j.ijplas.2016.09.001.

[40] B. Wu, N. Vajragupta, J. Lian, U. Hangen, P. Wechsuwanmanee, S. Münstermann, Prediction of plasticity and damage initiation behaviour of C45E + N steel by micromechanical modelling, Mater. Des. 121 (2017) 154–166, http://dx.doi.org/10.1016/j.matdes.2017.02.032.

[41] M.A. Wollenweber, S. Medghalchi, L.R. Guimarães, N. Lohrey, C.F. Kusche, U. Kerzel, T. Al-Samman, S. Korte-Kerzel, On the damage behaviour in dual-phase DP800 steel deformed in single and combined strain paths, Mater. Des. 231 (2023) 112016, http://dx.doi.org/10.1016/j.matdes.2023.112016.

[42] C. Kusche, T. Reclik, M. Freund, T. Al-Samman, U. Kerzel, S. Korte-Kerzel, Large-area, high-resolution characterisation and classification of damage mechanisms in dual-phase steel using deep learning, PloS One 14 (5) (2019) e0216493, http://dx.doi.org/10.1371/journal.pone.0216493.

[43] F. Roters, M. Diehl, P. Shanthraj, P. Eisenlohr, C. Reuber, S.L. Wong, T. Maiti, A. Ebrahimi, T. Hochrainer, H.-O. Fabritius, S. Nikolov, M. Friák, N. Fujita, N. Grilli, K. Janssens, N. Jia, P. Kok, D. Ma, F. Meier, E. Werner, M. Stricker, D. Weygand, D. Raabe, DAMASK – the Düsseldorf advanced material simulation kit for modeling multi-physics crystal plasticity, thermal, and damage phenomena from the single crystal up to the component scale, Comput. Mater. Sci. 158 (2019) 420–478, http://dx.doi.org/10.1016/j.commatsci.2018.04.030.

[44] J.R. Rice, Inelastic constitutive relations for solids: An internal-variable theory and its application to metal plasticity, J. Mech. Phys. Solids 19 (6) (1971) 433–455, http://dx.doi.org/10.1016/0022-5096(71)90010-X.

[45] J.W. Hutchinson, Bounds and self-consistent estimates for creep of polycrystalline materials, Proc. R. Soc. A 348 (1652) (1976) 101–127, http://dx.doi.org/10.1098/rspa.1976.0027.

[46] D. Peirce, R.J. Asaro, A. Needleman, An analysis of nonuniform and localized deformation in ductile single crystals, Acta Metall. 30 (6) (1982) 1087–1119, http://dx.doi.org/10.1016/0001-6160(82)90005-0.

[47] D. Peirce, R.J. Asaro, A. Needleman, Material rate dependence and localized deformation in crystalline solids, Acta Metall. 31 (12) (1983) 1951–1976, http://dx.doi.org/10.1016/0001-6160(83)90014-7.

[48] P. Shanthraj, B. Svendsen, L. Sharma, F. Roters, D. Raabe, Elasto-viscoplastic phase field modelling of anisotropic cleavage fracture, J. Mech. Phys. Solids 99 (2017) 19–34, http://dx.doi.org/10.1016/j.jmps.2016.10.012.

[49] F. Roters, P. Eisenlohr, L. Hantcherli, D.D. Tjahjanto, T.R. Bieler, D. Raabe, Overview of constitutive laws, kinematics, homogenization and multiscale methods in crystal plasticity finite-element modeling: Theory, experiments, applications, Acta Mater. 58 (4) (2010) 1152–1211, http://dx.doi.org/10.1016/j.actamat.2009.10.058.

[50] F. Roters, D. Raabe, G. Gottstein, Work hardening in heterogeneous alloys—a microstructural approach based on three internal state variables, Acta Mater. 48 (17) (2000) 4181–4189, http://dx.doi.org/10.1016/S1359-6454(00)00289-5.

[51] A. Ma, F. Roters, A constitutive model for fcc single crystals based on dislocation densities and its application to uniaxial compression of aluminium single crystals, Acta Mater. 52 (12) (2004) 3603–3612, http://dx.doi.org/10.1016/j.actamat.2004.04.012.

[52] C. Tian, D. Ponge, L. Christiansen, C. Kirchlechner, On the mechanical heterogeneity in dual phase steel grades: Activation of slip systems and deformation of martensite in DP800, Acta Mater. 183 (2020) 274–284, http://dx.doi.org/10.1016/j.actamat.2019.11.002.

[53] M. Henrich, N. Fehlemann, F. Bexter, M. Neite, L. Kong, F. Shen, M. Könemann, M. Dölz, S. Münstermann, DRAGen - a deep learning supported RVE generator framework for complex microstructure models, Heliyon 9 (8) (2023) e19003, http://dx.doi.org/10.1016/j.heliyon.2023.e19003.

[54] N. Fehlemann, Y. Sparrer, F. Pütz, M. Konemann, S. Münstermann, Influence of synthetically generated inclusions on the stress accumulation and concentration in X65 pipeline steel, IOP Conf. Ser.: Mater. Sci. Eng. 1157 (1) (2021) 012056, http://dx.doi.org/10.1088/1757-899X/1157/1/012056.

[55] F. Pütz, N. Fehlemann, V. Göksu, M. Henrich, M. Könemann, S. Münstermann, A data driven computational microstructure analysis on the influence of martensite banding on damage in DP-steels, Comput. Mater. Sci. 218 (2023) 111903, http://dx.doi.org/10.1016/j.commatsci.2022.111903.

[56] J. Schindelin, I. Arganda-Carreras, E. Frise, V. Kaynig, M. Longair, T. Pietzsch, S. Preibisch, C. Rueden, S. Saalfeld, B. Schmid, J.-Y. Tinevez, D.J. White, V. Hartenstein, K. Eliceiri, P. Tomancak, A. Cardona, Fiji: an open-source platform for biological-image analysis, Nature Methods 9 (7) (2012) 676–682, http://dx.doi.org/10.1038/nmeth.2019.

[57] N. Fehlemann, A.L. Suarez Aguilera, S. Sandfeld, F. Bexter, M. Neite, D. Lenz, M. Könemann, S. Münstermann, Identification of martensite bands in dual–phase steels: A deep learning object detection approach Using Faster Region–based–convolutional neural network, Steel Res. Int. 94 (7) (2023) http://dx.doi.org/10.1002/srin.202200836.

[58] F. Bachmann, R. Hielscher, H. Schaeben, Grain detection from 2d and 3d EBSD data–specification of the MTEX algorithm, Ultramicroscopy 111 (12) (2011) 1720–1733, http://dx.doi.org/10.1016/j.ultramic.2011.08.002.

[59] W. Liu, J. Lian, N. Aravas, S. Münstermann, A strategy for synthetic microstructure generation and crystal plasticity parameter calibration of fine-grain-structured dual-phase steel, Int. J. Plast. 126 (2020) 102614, http://dx.doi.org/10.1016/j.ijplas.2019.10.002.

[60] J. Kuhn, J. Spitz, P. Sonnweber-Ribic, M. Schneider, T. Böhlke, Identifying material parameters in crystal plasticity by Bayesian optimization, Optim. Eng. 23 (3) (2022) 1489–1523, http://dx.doi.org/10.1007/s11081-021-09663-7.

[61] T. Sakaki, K. Sugimoto, T. Fukuzato, Role of internal stress for continuous yielding of dual-phase steels, Acta Metall. 31 (10) (1983) 1737–1746, http://dx.doi.org/10.1016/0001-6160(83)90172-4.

[62] J. Kadkhodapour, A. Butz, S. Ziaei Rad, Mechanisms of void formation during tensile testing in a commercial, dual-phase steel, Acta Mater. 59 (7) (2011) 2575–2588, http://dx.doi.org/10.1016/j.actamat.2010.12.039.

[63] J.R. Greer, J.T. de Hosson, Plasticity in small-sized metallic systems: Intrinsic versus extrinsic size effect, Prog. Mater. Sci. 56 (6) (2011) 654–724, http://dx.doi.org/10.1016/j.pmatsci.2011.01.005.

[64] M.D. Uchic, P.A. Shade, D.M. Dimiduk, Plasticity of micrometer-scale single crystals in compression, Annu. Rev. Mater. Res. 39 (1) (2009) 361–386, http://dx.doi.org/10.1146/annurev-matsci-082908-145422.

[65] A.S. Schneider, D. Kaufmann, B.G. Clark, C.P. Frick, P.A. Gruber, R. Mönig, O. Kraft, E. Arzt, Correlation between critical temperature and strength of small-scale bcc pillars, Phys. Rev. Lett. 103 (10) (2009) 105501, http://dx.doi.org/10.1103/PhysRevLett.103.105501.

[66] O. Kraft, P.A. Gruber, R. Mönig, D. Weygand, Plasticity in confined dimensions, Annu. Rev. Mater. Res. 40 (1) (2010) 293–317, http://dx.doi.org/10.1146/annurev-matsci-082908-145409.

[67] C. Tian, C. Kirchlechner, The fracture toughness of martensite islands in dual-phase DP800 steel, J. Mater. Res. 36 (12) (2021) 2495–2504, http://dx.doi.org/10.1557/s43578-021-00150-4.

[68] J. Ast, M. Göken, K. Durst, Size-dependent fracture toughness of tungsten, Acta Mater. 138 (2017) 198–211, http://dx.doi.org/10.1016/j.actamat.2017.07.030.

[69] S. Wurster, C. Motz, R. Pippan, Characterization of the fracture toughness of micro-sized tungsten single crystal notched specimens, Phil. Mag. 92 (14) (2012) 1803–1825, http://dx.doi.org/10.1080/14786435.2012.658449.

[70] A.P. Ruybalid, J.P.M. Hoefnagels, O. van der Sluis, M.G.D. Geers, Comparison of the identification performance of conventional FEM updating and integrated DIC, Internat. J. Numer. Methods Engrg. 106 (4) (2016) 298–320, http://dx.doi.org/10.1002/nme.5127.